How much tropical cyclone intensification can result from the energy released inside of a convective burst?

Owen A. Kelley[1,2] and Jeffrey B. Halverson[3]

Received 15 March 2011; revised 19 July 2011; accepted 20 July 2011; published 25 October 2011.

[1] This study proposes a framework for estimating how much tropical cyclone intensification could result from the amount of energy released inside of a convective burst. A convective burst is a sequence of vigorous convective cells occupying one portion of a tropical cyclone's eyewall for approximately 9 to 24 h. On the basis of Tropical Rainfall Measuring Mission (TRMM) satellite radar observations and previous modeling studies, a typical convective burst may release in 12 h an extra 6×10^{17} J of latent heat. TRMM observations suggest that this extra energy represents an increase of 25% or more in the rate that the eyewall releases latent heat prior to the convective burst. Previous studies suggest that 4.5% to 11% of this extra latent heat may be transformed, after a lag of several hours, into an increase in the kinetic energy of the tropical cyclone's inner-core tangential wind. On the basis of the H*wind analysis of aircraft and dropsonde observations, an increase in kinetic energy of this magnitude may be associated with an intensification of 9–16 m s^{-1} (17–31 kt) in a tropical cyclone's maximum surface wind. This conservative estimate takes into account the increase in ocean surface friction during the period of intensification and assumes that the associated increase in ocean surface enthalpy flux does not counteract any of the frictional loss. Despite sources of uncertainty, it still appears that significant intensification is possible from the amount of energy released inside of a typical convective burst.

Citation: Kelley, O. A., and J. B. Halverson (2011), How much tropical cyclone intensification can result from the energy released inside of a convective burst?, *J. Geophys. Res.*, *116*, D20118, doi:10.1029/2011JD015954.

1. Introduction

[2] *Malkus and Riehl* [1960] and *Riehl and Malkus* [1961] hypothesized that a tropical cyclone is maintained by the latent heat released inside of convective cells in the eyewall. A series of particularly vigorous cells in one portion of the eyewall is commonly called a "convective burst" [*Hennon*, 2006]. A number of studies have found that convective bursts persist for at least 9 h and rarely longer than 24 h [*Steranka et al.*, 1986].

[3] *Rogers* [2010], *Braun et al.* [2006], and others have modeled convective bursts and associate intensification. Other studies suggest that convective bursts arise from random instabilities that cannot be predicted by tropical cyclone forecast models [*Van Sang et al.*, 2008, p. 580; *Shin and Smith*, 2008, p. 1670; *Montgomery et al.*, 2009]. An observational link between convective bursts and intensification has been found in statistical analyses of passive microwave [*Hennon*, 2006], infrared [*Steranka et al.*, 1986], and lightning observations [*Lyons and Keen*, 1994]. In addition, the link has been found in case studies of individual tropical cyclones, using microwave [*Rodgers et al.*, 2000; *Ritchie et al.*, 2003], radar [*Heymsfield et al.*, 2001; *Guimond et al.*, 2010; *Reasor et al.*, 2009], and lightning observations [*Fierro et al.*, 2011].

[4] Following the lead of studies such as *Malkus and Riehl* [1960] and *Montgomery et al.* [2009], this study hypothesizes that the energy to intensify the tropical cyclone passes through the convective burst. This idea likens the convective burst to an energy "pipeline." As an alternative to the pipeline analogy, the convective burst might change the spatial distribution of kinetic energy already in the tropical cyclone. This second option treats the convective burst as a "reorganizing agent," and evidence consistent with this option comes from this study's examination of the H*wind analysis.

[5] The goal of this study is to propose a framework for estimating the amount of intensification that might result from the energy released inside of a typical convective burst under the energy pipeline analogy. Previous studies support the energy pipeline analogy by invoking forced subsidence or vorticity. As shown schematically in Figure 1, vigorous convective cells in the eyewall have been observed to cause substantial subsidence, sometimes deep in the tropical cyclone's eye, which could warm the eye [*Heymsfield et al.*, 2001, p. 1311; *Schubert et al.*, 2007; *Guimond et al.*, 2010, Figure 4; *Molinari and Vollaro*, 2010, p. 3882]. Following

[1]NASA Goddard Space Flight Center, Greenbelt, Maryland, USA.
[2]Center for Earth Observing and Space Research, George Mason University, Fairfax, Virginia, USA.
[3]Joint Center for Earth Systems Technology, University of Maryland Baltimore County, Baltimore, Maryland, USA.

Copyright 2011 by the American Geophysical Union.
0148-0227/11/2011JD015954

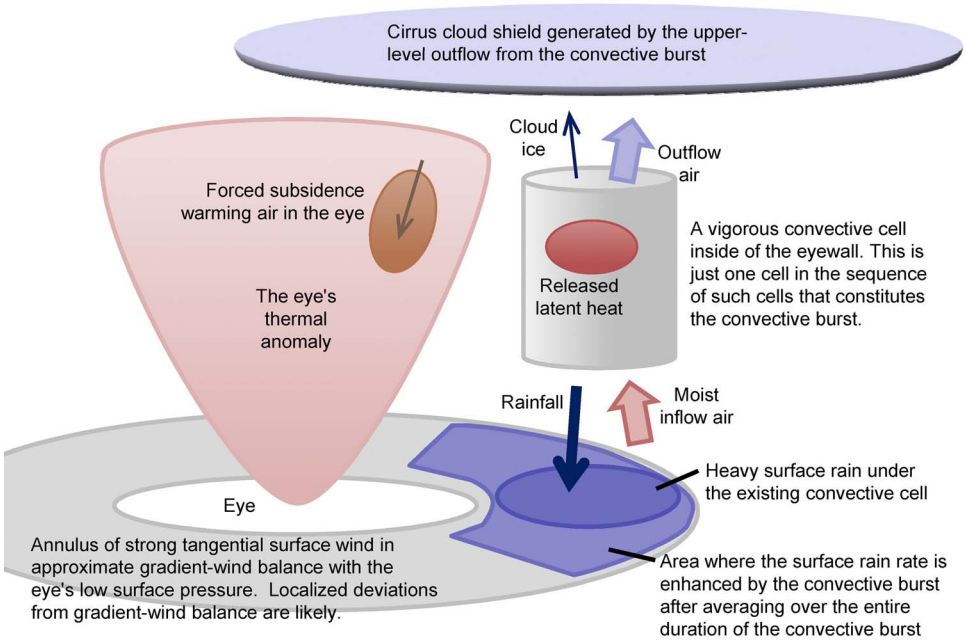

Figure 1. A schematic diagram of a vigorous convective cell in the eyewall of a tropical cyclone. A convective burst is a sequence of such convective cells.

such a warming, the eye's surface pressure would drop through hydrostatic adjustment. The tangential wind outside of the eye would speed up to reestablish approximate gradient wind balance with the new, lower central pressure [*Willoughby*, 1998]. Another candidate mechanism is that a vigorous cell transports vorticity into the eyewall. Some of the additional vorticity later becomes mixed azimuthally around the eyewall, increasing intensity [*Montgomery et al.*, 2006].

[6] This study puts together recent observations and modeling results to make a rough estimate of intensification using the three steps that are outlined below and in the block diagram (Figure 2). The first of these three steps is to estimate the amount of latent heat released inside of a convective burst in excess of the amount of latent heat normally released inside of the eyewall when no convective burst is present. Satellite radar observations during the past decade provide statistics on the amount of rainfall that falls out of a convective burst, which to a first approximation is proportional to the net condensation and therefore also proportional to the net latent heat release. The second step is to estimate what portion of the extra latent heat release may be converted into increased kinetic energy of the tangential wind. The recent modeling work of *Nolan et al.* [2007] provides such an efficiency. The third step is to consider how the kinetic energy increase is distributed throughout the three-dimensional structure of the tropical cyclone's inner-core tangential wind field. This study uses the H*wind analysis of *Powell et al.* [1998, 2010] to map kinetic energy increase to intensity increase.

2. Method

[7] Section 2 constructs the equations that implement the three-step process described in the Introduction section and in the block diagram (Figure 2). These equations have parameters whose values are estimated in section 3 and are listed in Table 1.

2.1. Released Energy

[8] Satellite observations of the surface rain rate provide a means to estimate the net column-integrated latent heat release inside of a convective burst. Latent heat is released in the eyewall even in the absence of a convective burst, so the quantity of interest is really the extra amount of latent heat released in the eyewall due to the presence of a convective burst.

[9] Section 3.1 suggests that a typical convective burst increases the surface rain rate by approximately 40 mm h^{-1} when averaging over a 500 km^2 area of the eyewall and over the duration of the convective burst. Even after averaging over the 500 km^2 area, the enhancement to the surface rain rate will still vary with respect to time as the convective burst becomes more or less active. Any such fluctuations will not affect the results of this study, as long as 40 mm h^{-1} is the mean enhancement to the surface rain rate after averaging over both space and time.

[10] To calculate latent heat release, one must first convert to different units the convective burst's enhancement to the surface rain rate ΔR (mm h^{-1}). To convert to rain mass flux F_{precip} (g m^{-2} s^{-1}), the partial canceling of a space factor of 1000 with a time factor of 3600 results in a coefficient of 5/18:

$$F_{precip}\left[\frac{\mathrm{g}}{\mathrm{m^2\,s}}\right] = \frac{1\mathrm{g}}{1.0\,\mathrm{cm^3}}\,\frac{10^6\,\mathrm{cm^3}}{1\,\mathrm{m^3}}\,\frac{1\,\mathrm{m}}{10^3\,\mathrm{mm}}\,\frac{1\,\mathrm{h}}{3600\,\mathrm{s}}\,\Delta R\left[\frac{\mathrm{mm}}{\mathrm{h}}\right],$$

$$F_{precip} = \frac{5}{18}\,\Delta R. \tag{1}$$

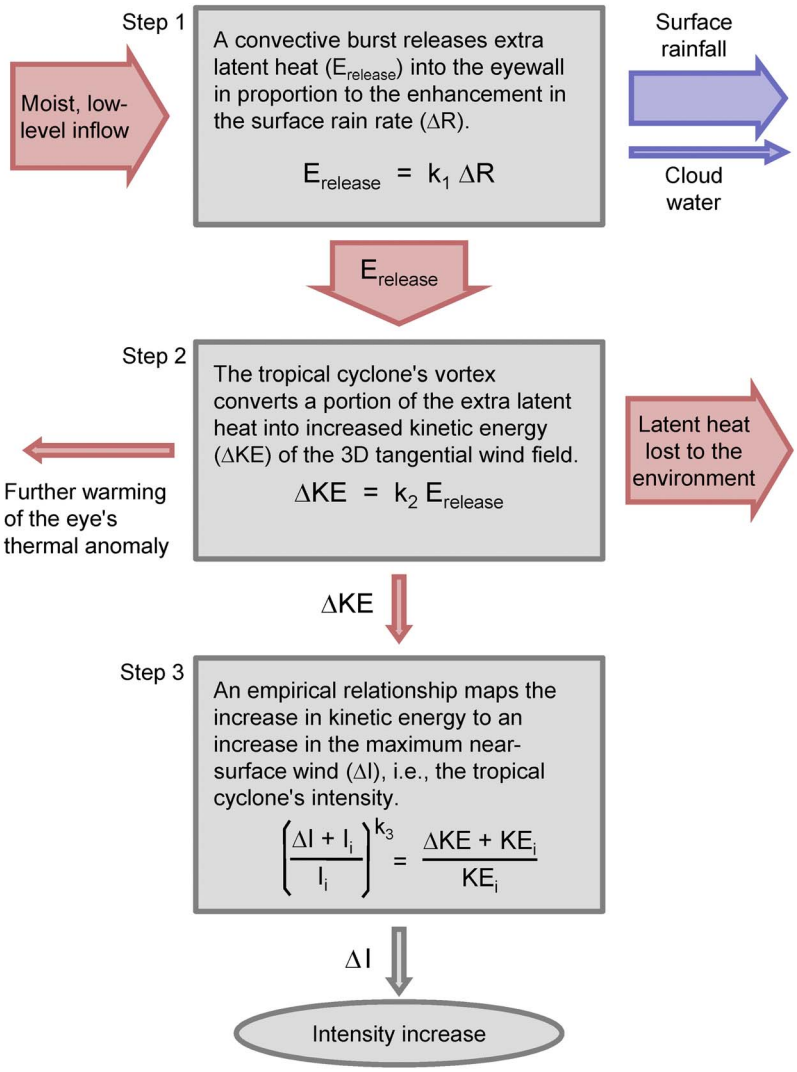

Figure 2. The framework that this study proposes for estimating intensification. The three steps in this framework are described in greater detail in section 2.

[11] Multiplying the rain mass flux by duration t_{burst} (s) and ocean surface area A_{burst} (m^2) gives the extra mass M_{precip} (g) of rain that reaches the ocean surface:

$$M_{precip} = F_{precip} A_{burst} t_{burst}. \quad (2)$$

[12] Rather than falling out as rain, some of the net condensation exits the convective burst as cloud ice in the upper-level outflow (Figure 1). This ice is observed as the large cirrus cloud shield that often obscures a satellite's view of the inner core during a convective burst [*Gentry et al.*, 1970]. Section 3.1 estimates that only about 10% of the eyewall's net condensation exits the eyewall as cloud ice.

[13] One arrives at the extra latent heat $E_{release}$ (J) by multiplying the net condensate mass by the specific heat of vaporization L_v (2.5×10^3 J g^{-1}). This calculation completes the first step in the block diagram (Figure 2). As equation (3) shows, either the precipitation mass can be scaled up by a factor f_{precip} of 1.1 to take into account the ~10% of the net condensate that leaves as cloud ice or the cloud ice M_{cloud} (g) can be explicitly included in the equation:

$$E_{release} = (M_{precip} + M_{cloud}) L_v = M_{precip} f_{precip} L_v. \quad (3)$$

[14] Using equation (3) and the parameters in Table 1 results in the convective burst releasing an extra 6.6×10^{17} J of latent heat during 12 h, beyond what the eyewall of a typical tropical cyclone releases when no convective burst exists. To put this value in context, section 3.2 analyzes Tropical Rainfall Measuring Mission (TRMM) satellite observations and finds that the convective burst's extra 6.6×10^{17} J of latent heat release represents a greater than 40% increase over the amount of latent heat that a weak tropical cyclone's eyewall would have released in 12 h and a greater than 25% increase over what a strong tropical cyclone's eyewall would have released in 12 h. In this text, "weak" means a minimal category 2 tropical cyclone and "strong" means minimal category 5 tropical cyclone on the

Table 1. Input Parameters for Estimating the Intensification That Could Result From the Amount of Energy Released Inside of a Typical Convective Burst

Quantity	Symbol	Point Value[a]	Range[b]
Amount by which the surface rain rate under the convective burst exceeds the surface rain rate in the eyewall in the absence of a convective burst[c]	ΔR	40 mm h^{-1}	27–60 mm h^{-1}
Horizontal cross-sectional area of the convective burst[c]	A_{burst}	500 km^2 (500 × 10^6 m^2)	333–750 km^2
Duration of the convective burst[d]	t_{burst}	12 h (4.32 × 10^4 s)	—
The ratio of water condensing in the convective burst to rainwater reaching the ocean's surface[e]	f_{rain}	1.1	1.05–1.15
Fraction of latent heat released in the convective burst can be used to cause tropical cyclone wind intensification[f]	f_{usable}	0.045, 0.11	0.030–0.067, 0.073–0.165
Initial kinetic energy of the tangential wind[g]	KE_i	5.1 × 10^{16} J, 1.1 × 10^{17} J	2.6 × 10^{16} − 1.0 × 10^{17} J, 5.5 × 10^{16} − 2.2 × 10^{17} J
Initial frictional flux of energy lost to the ocean surface[g]	F_i	9.1 × 10^{11} J s^{-1}, 2.8 × 10^{12} J s^{-1}	4.6 × 10^{11} − 1.8 × 10^{12} J s^{-1}, 1.4 × 10^{12} − 5.6 × 10^{12} J s^{-1}
Exponent relating intensity change to change in the kinetic energy of the tangential wind[g]	e_2	1.34	1.22–1.47
The exponent relating intensity change to change in the frictional dissipation rate at the ocean's surface[g]	e_3	2.12	1.93–2.33

[a]The point value is used to estimate intensification in section 2. When two values are provided, the first is for a borderline category 1–2 tropical cyclone with 42 m s^{-1} (82 kt) initial intensity and the second is for a borderline category 4–5 tropical cyclone with 70 m s^{-1} (135 kt) initial intensity. When the units used in the calculation are different than the units used in the text, the value expressed in computational units is provided in parentheses.
[b]The range is used in the error analysis in section 3.5.
[c]Based on the TRMM analysis in section 3.1.
[d]A typical duration based on *Hennon* [2006] and *Steranka et al.* [1986]. During error propagation in section 3.5, it is assumed that there is no error in the duration.
[e]From *Braun* [2006, p. 59] and *Gamache et al.* [1993, p. 3239].
[f]Based on results in or extrapolations from *Nolan et al.* [2007].
[g]Based on the examination of the H*wind analysis in sections 3.2 and 3.3.

Saffir-Simpson scale. By this criteria, weak and strong tropical cyclones have a 42 and 70 m s^{-1} (82 to 135 kt) intensity, respectively. Section 3 takes intensity to be the maximum wind reported in the 2-D surface field of the H*wind analysis, but the equations derived in section 2 are agnostic about where one obtains intensity estimates, either from H*wind, from National Hurricane Center best-track data, or from some other source.

[15] Section 3.1 estimates the fraction f_{usable} (unitless) of the extra latent heat release that may be converted into increased kinetic energy of the tropical cyclone's tangential wind. After multiplying the released energy by f_{usable}, the result is the energy E_{usable} (J) that can be used to increase kinetic energy:

$$E_{usable} = f_{usable} E_{release}. \tag{4}$$

Equation (4) completes the second step in the block diagram (Figure 2).

2.2. Intensification Ignoring the Increase in Friction

[16] The last step in the block diagram (Figure 2) is to map the increase in kinetic energy to an increase in intensity. Loosely following *Maclay et al.* [2008, equation (3)], this study uses a power law to match the fractional change in intensity to the fractional change in kinetic energy. The power law exponent e_2 (unitless) maps the final and initial kinetic energy, KE_f and KE_i (J), to the final and initial intensity, I_f and I_i (m s^{-1}):

$$\frac{KE_f}{KE_i} = \left(\frac{I_f}{I_i}\right)^{e_2}. \tag{5}$$

[17] Kinetic energy is estimated from the H*wind surface wind field, and intensity is taken to be the maximum of the H*wind surface wind field. In section 3.3, exponent e_2 is estimated by integrating out to a 70 km radius. To test the sensitivity of the integration limit, the integration was repeated with a 100 km radius and there was little change in the intensification. *Nolan et al.* [2007] used 50% to 150% of the radius of maximum wind as the radial limit of integration and also found that the integration limit had little effect on the resulting intensification.

[18] Next, equation (5) is manipulated algebraically to create equation (6). Equation (6) is a better equation for determining the intensification that results from the amount of energy released inside of a convective burst:

$$\Delta KE = KE_i(y^{e_2} - 1). \tag{6}$$

Equation (6) expresses the change in inner-core kinetic energy ΔKE (J) using a ratio y (unitless) between final and initial intensity, defined as follows:

$$\Delta KE = KE_f - KE_i, \qquad y = \frac{I_f}{I_i}. \tag{7}$$

[19] It is easy to solve for the intensity change by replacing ΔKE in equation (6) with E_{usable} and then solving the resulting equation for y:

$$E_{usable} = KE_i(y^{e_2} - 1), \tag{8a}$$

$$y = \left(1 + \frac{E_{usable}}{KE_i}\right)^{\frac{1}{e_2}}. \tag{8b}$$

[20] The parameters in equation (8b) other than y have values that are estimated in section 3 and stated in Table 1. Substituting these values into equation (8b) gives an intensification of 14 or 27 m s^{-1} (27 or 52 knots) for a weak or strong tropical cyclone, respectively.

[21] The 12-h 14–27 m s^{-1} intensification proposed in this section would qualify, or at least comes close to qualifying, as rapid intensification even if no further intensification occurred during the rest of the 24-h period. A commonly cited definition of rapid intensification is 15.4 m s^{-1} in 24 h, which was first proposed by *Kaplan and DeMaria* [2003, p. 1106]. Kaplan and DeMaria chose this threshold because it was at the 95th percentile of 24-h intensity change in North Atlantic tropical cyclones.

2.3. Intensification Considering the Increase in Friction

[22] While section 2.2 and *Nolan et al.* [2007, p. 3380] omit this effect, ocean surface friction does increase when intensity begins to increase. This section considers that during the period that intensity is increasing, some of the added energy will end up lost due to the wind-induced increase in friction. This energy loss reduces the intensification from what was estimated in section 2.2.

[23] Appendix A integrates the increase in frictional flux over the duration of the intensification period to come up with an estimate of the extra ocean surface frictional energy loss, $\Delta E_{friction}$ (J). Subtracting $\Delta E_{friction}$ from E_{usable}, as equation (9) does, is mathematically equivalent to reducing E_{usable} by lowering efficiency factor f_{usable} in equation (4):

$$E_{usable} - \Delta E_{friction} = KE_i(y^{e_2} - 1). \tag{9}$$

[24] This study chooses to handle friction by subtracting $\Delta E_{friction}$ so that this study can employ in equation (4) a value for the efficiency factor based on the constant friction results of *Nolan et al.* [2007].

[25] The increasing-friction formulation (equation (9)) must be solved numerically to arrive at a value for y, the fractional change in intensity, because $\Delta E_{friction}$ is a function of y. Using the parameters in Table 1, the result is a weak tropical cyclone experiencing an intensification of 9 m s^{-1} (17 knots) from the amount of latent heat released inside of a typical convective burst during a 12 h period. A strong tropical cyclone experiences 16 m s^{-1} (31 knots) in 12 h from the same amount of latent heat release.

[26] This increasing-friction formulation actually overestimates the effect of the friction increase (and underestimates the intensification) because it ignores that the flux of enthalpy from the ocean surface into the boundary layer also immediately increases when the intensification period begins, just as friction immediately increases when intensification begins. Friction immediately works as a drag on wind speed, while enthalpy flux requires time (perhaps several hours) to work its way into free troposphere, be transformed into eye warming, and eventually help the tropical cyclone overcome the increased ocean surface friction.

[27] Another reason why the intensification may be underestimated in the increasing-friction formulation is that the increasing-friction formulation assumes that friction is purely detrimental to intensification. In contrast, *Smith et al.* [2009, p. 1323] suggest that increasing friction will increase the radial inflow of moisture into the eyewall which might invigorate convection, releasing more latent heat into the eyewall.

[28] In short, the 9–16 m s^{-1} increasing-friction estimate of this section and the 14–27 m s^{-1} constant friction estimate of the previous section might bracket the most realistic intensity increase. To be conservative, this study emphasizes the 9–16 m s^{-1} range.

3. The Observational and Modeling Basis for the Input Parameters' Values

3.1. Parameters Related to Latent Heat Release

[29] This section describes how observations and modeling studies are used to choose typical values for the latent heating parameters that are used in the equations in section 2.1 and that are listed at the top of Table 1.

[30] Each of 136 TRMM satellite overflights of tropical cyclone eyewalls is categorized as containing or not containing a convective burst based on whether the eyewall has a $\geq 4 \times 10^4$ km^2 area of 11 μm infrared brightness temperature $\leq$203 K (−70°C) and a minimum 85 GHz horizontally polarized passive-microwave brightness temperature of $\leq$190 K [*Hennon*, 2006, p. 12]. While this study conceives of a convective burst as a period of 12 h of enhanced convection, this section uses a single overflight of the TRMM satellite to segregate burst from nonburst cases. If a separate study were undertaken, patching together observations from multiple satellites and factoring in any calibration issues between them, then a more-or-less continuous coverage of near-simultaneous microwave and infrared observations would be possible. Were such a study performed, the separation of burst from nonburst cases might differ for some of the cases considered here.

[31] Among the 136 overflights, 42 are categorized as containing a convective burst. In all 136 overflights, the eyewall was completely observed by the TRMM Precipitation Radar, which provides the 5-km-resolution surface precipitation estimates used in this section [*Kozu et al.*, 2001; *Iguchi et al.*, 2009; *Seto and Iguchi*, 2007; http://www.eorc.jaxa.jp/TRMM]. The infrared and passive-microwave instruments on the TRMM satellite are described by *Kummerow et al.* [1998].

[32] In each of these overflights, the eyewall is located in the surface precipitation by manually choosing an inner and outer radius that encloses the eyewall's heavy surface precipitation. As will be described below, the TRMM radar reveals that most of the extra surface precipitation mass in burst versus nonburst cases occurs in the quarter of the eyewall (a 90° arc) with the heaviest average surface rainfall. Figure 3a shows the area of one quarter of the eyewall for the 42 convective burst cases. For these same cases, Figure 3c shows the surface rain rate averaged over this area. Figure 3d plots the corresponding rain rate average for the non-convective-burst cases, i.e., rain rate averaged over the 90° arc of the eyewall that has the highest average rain rate among all possible 90° arcs.

[33] The goal is to calculate the enhancement to the latent heat release in 12 h due to the presence of the convective burst, so the scatter of areas (Figures 3a–3b) and rain rate averages (Figures 3c–3d) are used to estimate the latent heat release (Figure 3f).

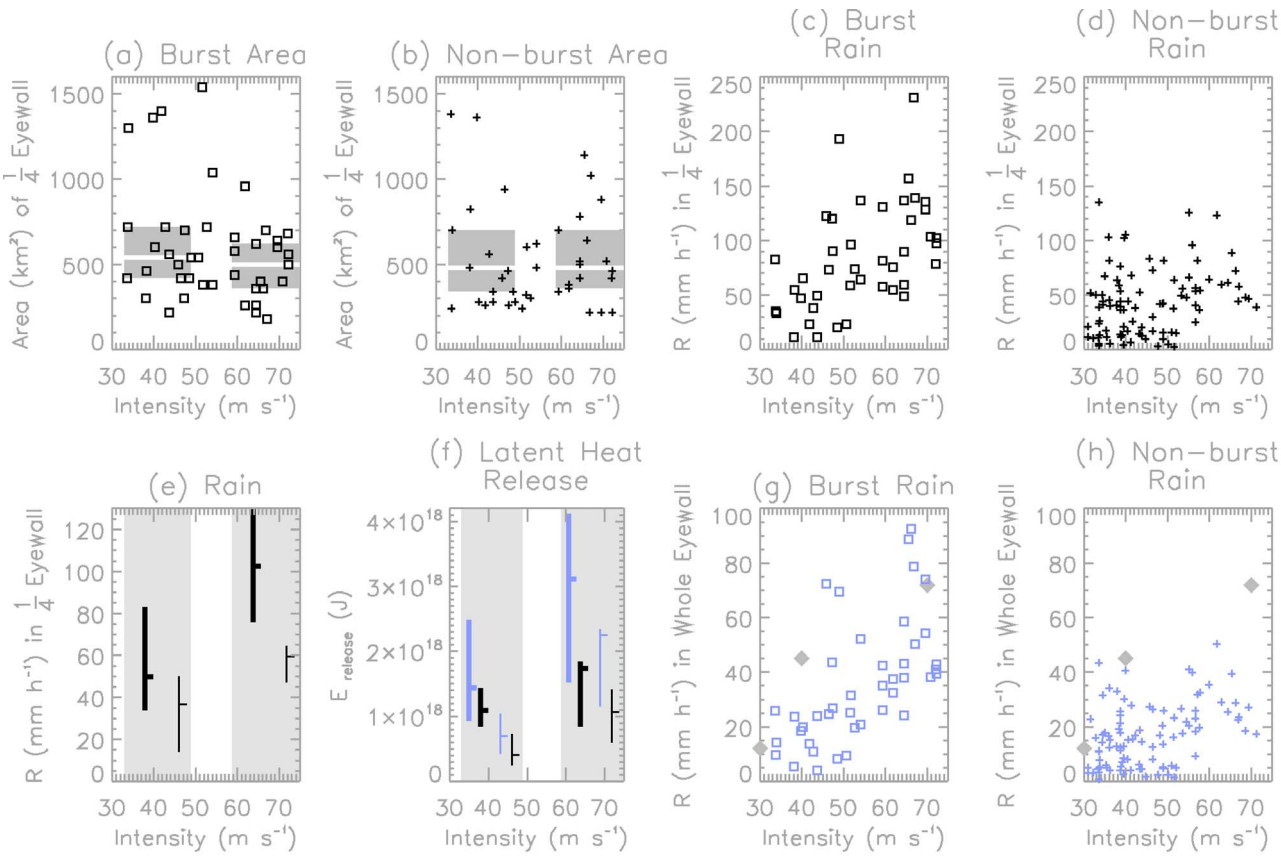

Figure 3. TRMM radar observations to estimate the additional amount of latent heat released in the tropical cyclone eyewall when a convective burst is present. (a) The area of one quarter of the eyewall, which this study takes to be the area occupied by the convective burst. The gray areas represent the middle 50% of the scatter for weak or strong tropical cyclones. The white horizontal line that divides each rectangle represents the median. (b) The same as Figure 3a except for eyewalls that do not contain a convective burst. (c) The TRMM Precipitation Radar average surface rain rate for the quarter of the eyewall with the highest average surface rain rate in 42 overflights of tropical cyclones experiencing a convective burst. (d) The same as in Figure 3c except for 96 overflights without a convective burst. (e) The thick and thin bars summarize the scatter of rainfall rates in Figures 3c and 3d. The top and bottom of the bars are the middle 50% of the scatter and the middle notch is the median of the scatter. The two gray regions indicate weak or strong tropical cyclones, i.e., tropical cyclones at intensity category 1 or 2 or at intensity category 4 or 5. (f) The black symbols summarize the net latent heat release in the quarter of the eyewall with the highest average surface rain rate, using equation (3). The blue symbols summarize the net latent heat release in the entire eyewall. The thick and thin symbols are for burst and nonburst cases, respectively. (g) The blue symbols show the scatter of average rainfall rates when averaging over the entire eyewall in the convective burst cases. The three gray diamonds show estimates of eyewall-average rainfall rates from *Langousis and Veneziano* [2009, Figure 5a]. (h) The same as Figure 3g except for eyewalls without convective bursts.

[34] Supporting a statement a few paragraphs earlier, Figure 3f shows that most of the extra latent heat released in the whole eyewall is actually released in just one quarter of the eyewall. To see this result, note that the median difference in latent heat release with and without a convective burst is similar whether one is looking at a quarter of the eyewall (black lines in Figure 3f) or one is looking at the entire eyewall (blue lines in Figure 3f). If one simplifies these results by taking the area of the convective burst to be 500 km^2, as is done in Table 1 and section 2.1, then that requires that one use a rainfall rate enhancement of ~40 mm h^{-1} in order to get a correct enhancement to the latent heat release.

[35] The eyewall rain rate estimated by the TRMM Precipitation Radar and shown in Figure 3 is higher than the rain rate estimated by the TRMM Microwave Imager (TMI). Averaging TMI observations of many tropical cyclones, *Lonfat et al.* [2004, Figure 11a] report that the average TMI rain rate is just 7 or 12 mm h^{-1} in the vicinity of the eyewall of a weak or strong tropical cyclone, respectively. *Langousis and Veneziano* [2009, p. 2] explain why the eyewall rain rate of the TRMM radar is likely to be more accurate than the lower rate estimated by TMI.

[36] As mentioned in section 2.1, it is difficult to improve on the estimate that ~10% of the convective burst's net condensate ends up as cloud ice that leaves in the upper-level

outflow (Table 1, fourth row). This 10% figure is based on the hurricane simulations of *Braun* [2006, p. 59] and the Doppler radar analysis of *Gamache et al.* [1993, p. 3239]. Other observations are in broad agreement with this 10% figure. For example, a large cloud shield might have 0.1 g kg^{-1} ice concentration, a 200 km radius, a 2 km depth, and thereby contain 2.5×10^{13} g of cloud ice, which is close to 10% of the 2.6×10^{14} g of precipitation mass estimated by equation (2). Sources of uncertainty in this estimate include the fact that the cloud-ice concentration in high-altitude, tropical, maritime/coastal clouds can be anything from 0.001–0.01 g kg^{-1} to ~0.3 g kg^{-1} (low estimates: *Heymsfield and Donner* [1990, Figure 5], *Knollenberg et al.* [1993, Figure 16]; high estimates: *Pueschel et al.* [1995, Figure 2], *Kelley et al.* [2010, Figure 5i]). Also, cirrus cloud shields are often smaller than this hypothesized 200 km radius [*Heymsfield et al.*, 2001, Figure 3; *Guimond et al.*, 2010, Figure 5]. The smaller cloud shield size may be due to cloud ice being subject to a 0.1–1.0 m s^{-1} fall speed [*Heymsfield and4 Iaquinta*, 2000, Figure 14a; *Schmitt and Heymsfield*, 2009, Figure 3], slow subsidence [*Kossin*, 2002, Figure 8], and evaporation after mixing with background cloud-free air above and below the cloud shield [*Houze*, 1993, pp. 180–182].

3.2. Parameters Related to Initial Kinetic Energy and Friction

[37] This section describes how typical values were identified for the kinetic energy and ocean surface frictional flux (Table 1, sixth and seventh rows). The kinetic energy *KE* (J) in question is the three-dimensional kinetic energy of the tropical cyclone's inner-core tangential wind (equation (10a); Figure 4a). Frictional flux *F* (J s^{-1}) is calculated by substituting the H*wind analysis into equation (10b), the bulk aerodynamic formula [*Emanuel*, 1997, equation (7); *Emanuel*, 2003, equation (5)], as shown in Figure 4b.

$$KE = \frac{1}{2} s_0 \, m \, A_{grid} \sum_{\substack{inner \\ core}} v_{700\,\mathrm{hPa}}^2 \tag{10a}$$

$$F = c_d \, \rho_0 \, A_{grid} \sum_{\substack{inner \\ core}} v_{surf}^3 . \tag{10b}$$

[38] The factors of the kinetic energy equation (equation (10a)) are listed in the order that they appear. Appendix B estimates s_0 (unitless), the parameterization of the vertical variation in tangential wind speed. The mass *m* (kg m^{-2}) of air in the tropospheric column from the surface to 12 km altitude is taken to be 80% of the total mass of a hydrostatic atmosphere with scale height *H* (8500 m) defined by *Bohren and Albrecht* [1998, p. 55–56]. In this study, the vertical integration is intentionally similar to the 2–12 km integration in the work of *Nolan et al.* [2007, p. 3401]. In this study, surface pressure under the eyewall is taken to be 970 hPa in both strong and weak tropical cyclones. *Holland* [1980, Figure 2a] suggests the 970 hPa value is approximately correct for moderate and strong tropical cyclones. The 970 hPa value is perhaps a ~15 hPa underestimate of eyewall surface pressure for a weak tropical cyclone, but it has little effect on the results of this study. The area of each grid box of the H*wind analysis is A_{grid} (m^2). The summation is over all the grid boxes within 70 km of the center of the eye, for reasons explained in the next section. The 700 hPa tangential wind speed $v_{700\mathrm{hPa}}$ (m s^{-1}) is here estimated as the H*wind surface wind speed divided by 0.85. *Powell et al.* [2009, Table 3] state that using a factor of 0.80 or 0.90 would overestimate or underestimate the difference between surface and 700 hPa wind speed, so this study uses a factor of 0.85.

[39] The factors of the frictional flux equation (equation (10b)) are listed in the order they appear. For the sake of simplicity, this study uses the same drag coefficient ($c_d = 2 \times 10^{-3}$) for weak and strong tropical cyclones following *Vickery et al.* [2009, Figure 3] and *Andreas and Emanuel* [2001, p. 3746]. Other studies have suggested lower values for c_d of 1.4×10^{-3} to 1.8×10^{-3} in weak tropical cyclones [*Powell et al.*, 2003] or 0.6×10^{-3} to 2.2×10^{-3} for strong tropical cyclones [*Soloviev and Lukas*, 2010, Figure 4]. The surface air density under the eyewall is ρ_o (kg m^{-3}). The surface wind speed as reported in the H*wind analysis is v_{surf} (m s^{-1}).

3.3. Parameters Related to Change in Kinetic Energy and Friction

[40] This section describes how typical values were identified for the power law exponents that map change in intensity to change in either kinetic energy or ocean surface friction (Table 1, eighth and ninth rows). Kinetic energy and ocean surface friction are integrated within a 70 km radius measured from the storm center.

[41] To calculate the typical kinetic energy increase associated with an intensity increase, pairs of H*wind analyses are compared 12 h apart using equation (10a). For each 12 h interval, the power law exponent e_2 is calculated using equation (5) as shown in Figure 4c. Table 1 (eighth row) reports the median value for the power law exponent during normal periods of intensification that are associated with increases in kinetic energy (the red symbols in Figure 4c).

[42] To calculate the typical increase in frictional flux associated with an intensity change, the analysis is repeated, this time using equation (10b) to calculate frictional flux and equation (A2) to calculate power law exponent e_3. The scatter of values for e_3 is shown in Figure 4d, with a typical value reported in Table 1 (ninth row).

[43] This study uses 27 twelve-hour intensification periods in the H*wind analysis to estimate the intensification that might result from the amount of energy released inside of a typical convective burst, conceiving of a convective burst as an energy pipeline. If changes in the spatial distribution of kinetic energy deviated from the typical, then much greater intensification could result. For example, five periods of intensification were excluded from the analysis because kinetic energy decreased (the green symbols in Figure 4c). Tables 2 and 3 and Figure 4g show that these five periods experienced greater intensification in the National Hurricane Center best track data than the intensification of the H*wind maximum wind. Either the kinetic energy is becoming more tightly concentrated at the radius of maximum winds or the overall area of the inner core is shrinking. The possibility of a shrinking radius of maximum winds is discussed by *Vickery and Wadhera* [2008, Figure 9], *Willoughby and Rahn* [2004, Figure 6], and *Smith et al.* [2009, Figure 7].

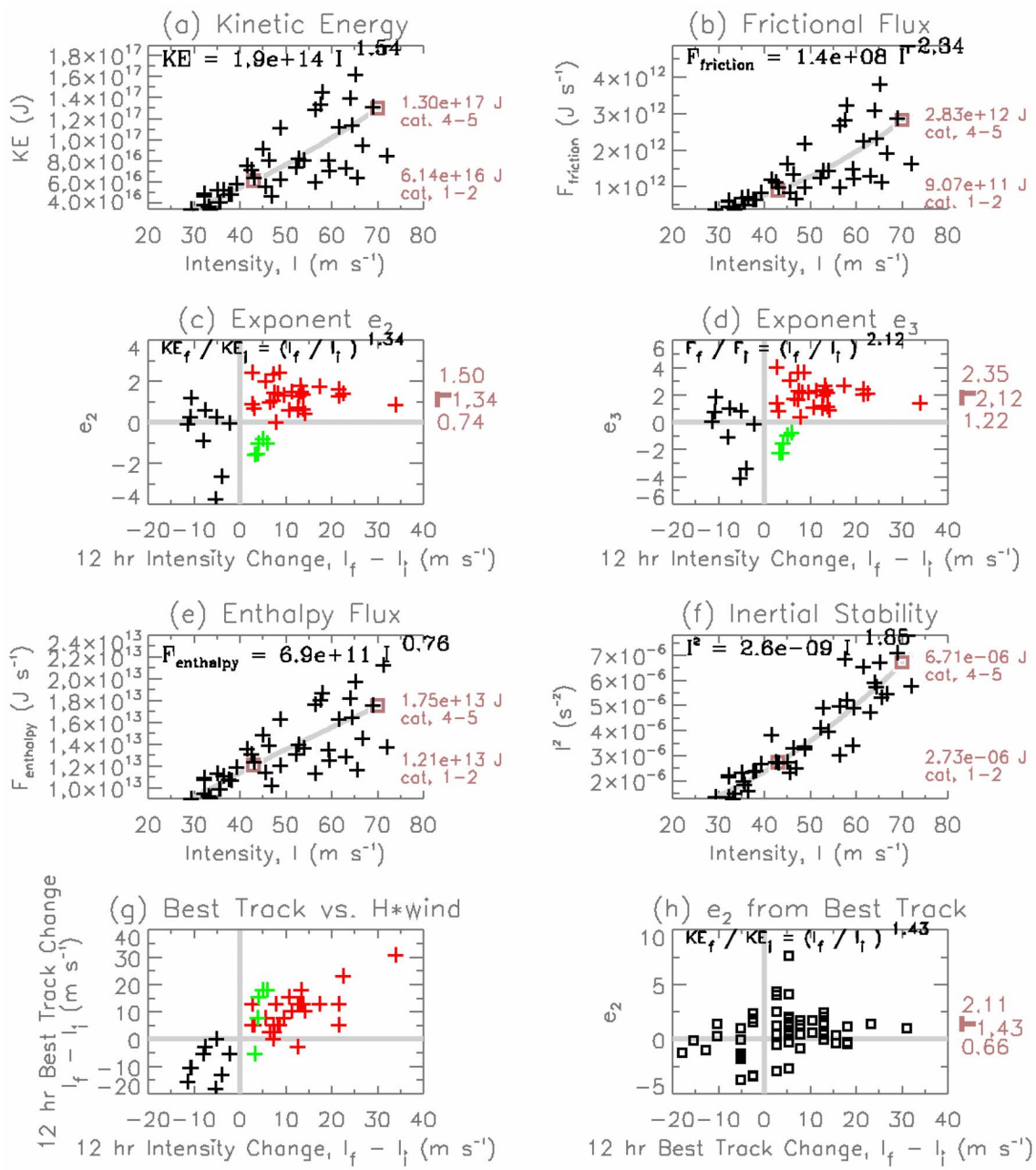

Figure 4. Three-dimensional tangential wind kinetic energy and ocean surface frictional flux as a function of either intensity or intensity change. The kinetic energy and frictional flux are estimated from the H*wind analysis within 70 km of the storm center for the North Atlantic tropical cyclones listed in the last seven rows of Table 2. (a) An estimate of the kinetic energy based on the H*wind analysis and a parameterization of the vertical variation in the tangential wind speed derived in Appendix B. (b) An estimate of the ocean surface frictional flux. (c) As defined in equation (5), the kinetic energy power law exponent e_2, calculated by fitting 12-h change in intensity to 12-h change in kinetic energy. The red symbols are for 12-h periods during which both intensity and kinetic energy increase. The 25th percentile, median, and 75th percentile of the scatter of red symbols are shown by the bottom, middle, and top of the bar to the right of the plot. The green symbols indicate the anomalous cases of intensity increase despite kinetic energy decrease. The black symbols represent periods of decreasing intensity and are therefore not used in this study but are included in the figure so that the same cases can be shown in all eight panels of this figure. (d) Same as in Figure 4c except for frictional flux as defined in equation (A2). (e) Enthalpy flux calculated using *Emanuel* [2003, equation (4)]. (f) Inertial stability as calculated in section 3.4. (g) This study uses the maximum H*wind speed as an estimate of intensity. Shown is the scatter of this value against the National Hurricane Center's best-track estimate of intensity. (h) The calculation of power law exponent e_2 repeated, this time using the best-track estimate of intensity.

Table 2. North Atlantic Tropical Cyclones for Which Previous Observational Studies Provide Estimates of the Vertical or Horizontal Variation in Tangential Wind Speed[a]

Hurricane Name	Date and Time of Observation	Data Source
Inez (1966)	27 and 28 Sep	Flight-level winds at 5 levels from 950 hPa to 180 hPa [*Hawkins and Imbembo*, 1976, Figure 4 and 13]
Guillermo (1997)	2130 and 2300 UTC, 2 Aug	Doppler radar [*Zou et al.*, 2010, Figure 4]
Ivan (2004)	1724–1751, 1802–1826 UTC 07 Sep, 1902–2727 UTC 14 Sep	Doppler radar [*Stern and Nolan*, 2009, Figure 2d]
Dennis (2005)	2445–2740 UTC 07 Jul, 1608–1952 UTC 10 Jul	Doppler radar [*Stern and Nolan*, 2009, Figure 5a]
Gilbert (1988)	0902–1016 UTC 14 Sep	Doppler radar [*Dodge et al.*, 1999, Figure 10]
Norbert (1984)	0 UTC 24 Sep	Doppler radar [*Marks et al.*, 1992, Figure 8a]
Gloria (1985)	0 UTC 25 Sep	Dropsondes and flight-level winds [*Franklin et al.*, 1993, Figure 10]
Katrina (2005)	1200 UTC 27 Aug to 0000 UTC 29 Aug	The H*wind analysis includes dropsondes, flight-level winds, and other observations [*Powell et al.*, 1998, 2010]
Emily (2005)	0730 UTC 14 Jul to 1330 UTC 17 Jul	The H*wind analysis includes dropsondes, flight-level winds, and other observations [*Powell et al.*, 1998, 2010]
Rita (2005)	0430 UTC 21 Sep to 0130 UTC 23 Sep	The H*wind analysis includes dropsondes, flight-level winds, and other observations [*Powell et al.*, 1998, 2010]
Dean (2007)	1930 UTC 17 Aug to 1930 UTC 19 Aug	The H*wind analysis includes dropsondes, flight-level winds, and other observations [*Powell et al.*, 1998, 2010]
Felix (2007)	1930 UTC 1 Sep to 1930 UTC 3 Sep	The H*wind analysis includes dropsondes, flight-level winds, and other observations [*Powell et al.*, 1998, 2010]
Omar (2008)	0430 UTC 15 Oct to 1330 UTC 16 Oct	The H*wind analysis includes dropsondes, flight-level winds, and other observations [*Powell et al.*, 1998, 2010]
Paloma (2008)	1930 UTC 6 Nov to 1330 UTC 8 Nov	The H*wind analysis includes dropsondes, flight-level winds, and other observations [*Powell et al.*, 1998, 2010]

[a]First seven hurricanes were used to generate the vertical profiles in Figure B1a. The last seven were used to generate Figure 4.

3.4. The Efficiency Parameter

[44] Linear perturbations in the tropical cyclone model of *Nolan et al.* [2007] explicitly result in 4.5% of the latent heat that is released nonsymmetrically in one portion of a weak tropical cyclone's eyewall being transformed by the vortex into increased kinetic energy of the tropical cyclone's tangential wind (Table 1, fifth row). Future studies may include nonlinear effects not modeled by Nolan et al. and refine the value of this efficiency factor.

[45] The rest of this section extrapolates Nolan's results to a strong tropical cyclone. One could simply fit a power law to Nolan's results for weak tropical cyclones and extend the line to strong tropical cyclones. Such a purely mathematical extrapolation gives an ~11% efficiency for strong tropical cyclones.

[46] A physics-based extrapolation gives close to the same answer as the purely mathematical extrapolation that was just described. One unplanned aspect of Nolan's model output for weak tropical cyclones is that the latent-heat-to-kinetic-energy conversion efficiency increases in proportion to the increase in the inertial stability of the tropical cyclone's vortex. If one assumes that such a proportionality is maintained in strong tropical cyclones, then the extrapolated efficiency for strong tropical cyclones (dotted line in Figure 5) is approximately the same as the previously stated 11% efficiency that is independent of any consideration of inertial stability.

[47] A rough proportionality between latent heat conversion and inertial stability is plausible, in a balanced axisymmetric vortex, because sufficiently gentle radial perturbations will give rise to waves that have a frequency that is less than or equal to the square root of the inertial stability [*Kepert*, 2010]. Incidentally, these waves are analogous gravity waves set up by vertical perturbations [*Kepert*, 2010, p. 5–6]. As inertial stability increases, the upper bound to the frequency of trapped radially forced waves increases, trapping a larger fraction of them. When a larger fraction of waves are trapped, one would expect more of the latent heat release to eventually be converted to inner-core kinetic energy.

[48] This study calculates density-weighted average 3-D inertial stability in the inner core for the H*wind analyses, as plotted in Figure 4f. Various studies use different formulas to calculate inertial stability. *Kepert* [2010, equation (19)] and *Fudeyasu and Wang* [2011, equation (4)] calculate inertial stability I^2 (s^{-2}) as the product of the absolute Coriolis parameter f_{abs} (s^{-1}) and the absolute vorticity ε (s^{-1}):

$$\begin{aligned} f_{abs} &= f_0 + 2\frac{v_\theta}{r}, \\ \varepsilon &= f_0 + \frac{\delta}{\delta r} v_\theta + \frac{v_\theta}{r} - \frac{1}{r}\frac{\delta}{\delta\theta} v_r, \\ I^2 &= f_{abs}\,\varepsilon. \end{aligned} \tag{11}$$

Table 3. Twelve-Hour Periods of Atlantic Tropical Cyclones During Which the Maximum H*Wind Speed Increases but the H*Wind Inner Core Kinetic Energy Decreases

Hurricane Name	Date and Start Time of 12-h Period	12-h Change in Intensity (m s^{-1})	
		H*Wind Change in Max Wind	Best-Track Change in Intensity
Felix (2007)	1930 UTC 02 Sep 2007	6.0	18.0
Rita (2005)	1730 UTC 21 Sep 2005	4.9	18.0
Paloma (2008)	1930 UTC 07 Nov 2008	4.0	15.5
Emily (2007)	0730 UTC 16 Jul 2007, 0130 UTC 17 Jul 2007	3.9, 3.3	7.7, −5.2

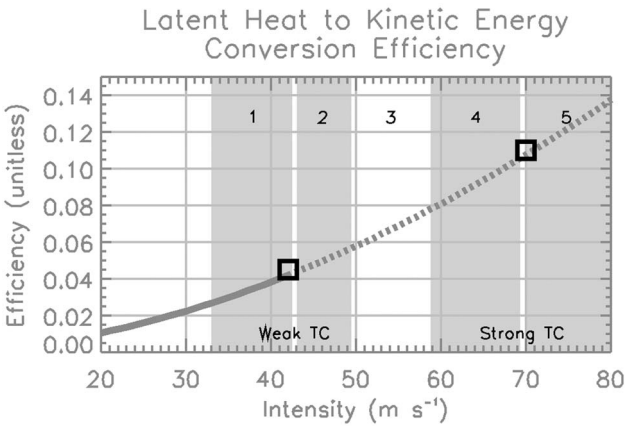

Figure 5. The tropical cyclone's efficiency at converting extra latent heat release into kinetic energy of the tangential wind. The solid line comes from *Nolan et al.* [2007, Figure 21a]. The dotted line is an extrapolation based on the inertial stability calculated from H*wind surface wind analyses plotted in Figure 4f. The two open squares are the 4.5% and 11% efficiency that this study uses for weak and strong tropical cyclones, respectively.

[49] *Shapiro and Montgomery* [1993] provide an expression for f_{abs}. In equation (11), f_0 (s^{-1}) is the planetary Coriolis parameter [*Wallace and Hobbs*, 2006, p. 277], v_θ (m s^{-1}) and v_r (m s^{-1}) are the tangential and radial components of the H*wind wind speed, $\delta/\delta\theta$ and δ/δr are the tangential and radial derivatives, and r (m) is the distance from the center of an H*wind grid box to the center of the tropical cyclone's eye. Because the H*wind analysis is not axisymmetric, this study includes in ε the $\delta/\delta\theta$ term of the vertical component of the curl of velocity, as does *Kepert* [2010, equation (15)]. In contrast, *Nolan et al.* [2007, equation (5.5)] can omit the $\delta/\delta\theta$ term because their wind field is axisymmetric after it adjusts to the added latent heat.

3.5. Input Parameter Uncertainty

[50] One can propagate uncertainty in input parameters to the estimate of usable energy E_{usable} (J) and then propagate uncertainty to the estimated intensification ΔI (m s^{-1}). Both E_{usable} and ΔI can be expressed as a function of their input parameters:

$$E_{usable} = f\left(\Delta R, A_{burst}, t_{burst}, f_{precip}, f_{usable}\right),$$
$$\Delta I = f\left(E_{usable}, KE_i, F_i, e_2, e_3\right). \tag{12}$$

[51] The propagation of errors formula can be found in the work of *Bevington and Robinson* [1992, p. 43]. The rightmost column of Table 1 lists uncertainty in the input parameters that implies, through error propagation, a factor of 2.3 uncertainty in the intensification rate. Under the conservative estimate of increased friction and no effect from increased enthalpy flux, the previously calculated point estimate is 9 m s^{-1} for a weak tropical cyclone and 16 m s^{-1} for a strong tropical cyclone. Applying the 2.3 uncertainty factor, these point estimates become 4–21 m s^{-1} for a weak tropical cyclone and 7–37 m s^{-1} for a strong tropical cyclone.

[52] Since rapid intensification is usually defined as 15.4 m s^{-1} in 24 h, then "half a day's worth" of rapid intensification would consist of 7.7 m s^{-1} in 12 h. Most of the weak tropical cyclone's 4–21 m s^{-1} intensification range is above 7.7 m s^{-1} and virtually all of a strong tropical cyclone's 7–37 m s^{-1} intensification range is as well. In summary, a 12-h-long convective burst can cause half a day's worth of rapid intensification if it avoids the least favorable combinations of parameter values.

4. Discussion

[53] This section explains why latent heat of vaporization is calculated in this study rather than other measures of energy. Only latent heat of vaporization (latent heat of condensation and evaporation) is calculated in the "released energy" equation, equation (3). In contrast, latent heat of fusion (latent heat released when water freezes) is omitted because heat of fusion is an insignificant fraction (~1%) of the net latent heating inside of a convective burst. Only 10% of the condensate freezes and remains frozen (equation (3)). The rest of the net condensate never freezes or remelts before it falls to the ocean surface. The specific latent heat of fusion ($L_f = 0.33 \times 10^3$ J g^{-1}) is only ~10% of the specific latent heat of vaporization ($L_v = 2.5 \times 10^3$ J g^{-1}). Combining these two factors of 10% result in the just-stated 1%.

[54] Even though latent heat of fusion is not explicitly included in the calculations, the authors acknowledge the great importance that freezing and melting can have on convective dynamics. Freezing and melting redistribute heat within the atmospheric column and do help convective cells to reach high altitude [*Zipser*, 2003]. In other words, latent heat of fusion is not explicitly included in the equations of this study, but it affects the efficiency factor f_{usable} in equation (4).

[55] *Emanuel* [2003, p. 84] describes a tropical cyclone as balancing enthalpy flux from the ocean with frictional loss at the ocean surface. Nonetheless, this study tracks latent heat instead of enthalpy (latent plus sensible heat) [*Glickman*, 2000]. The reason for preferring latent heat, in this context, is that this study uses the energy efficiency calculated by *Nolan et al.* [2007]. Nolan et al. use a vertical profile of heat release that is modeled after the vertical profile of latent heat release. As sections 2.2 and 2.3 have shown, the latent heat released by a convective burst appears, by itself, to be sufficient to cause significant intensification.

[56] Moist static energy is the sum of enthalpy and gravitational potential energy [*Bohren and Albrecht*, 1998, p. 290]. This study does not track intermediate exchanges between gravitational potential energy and other forms of energy as the released energy works its way toward becoming increased kinetic energy of tangential wind. Instead, intermediate transformations are summarized in this study by the use of an efficiency factor of latent heat release to kinetic energy increase, following the work of *Nolan et al.* [2007].

5. Conclusion

[57] The framework developed in this study represents a convective burst as an energy pipeline that carries extra latent heat up from the boundary layer and releases the latent heat into the free troposphere. A convective burst is simply a sequence of vigorous convective cells that occupies one portion of a tropical cyclone's eyewall for a period of at least 9 h and rarely longer than 24 h.

[58] This study estimates that a typical convective burst releases an extra 6.6×10^{17} J of latent heat every 12 h. TRMM satellite radar observations suggest a roughly equal boost to the latent heat release regardless of whether the convective burst occurs in a weak or strong tropical cyclone. This extra latent heat release represents an increase of 25% or more, on average, in the rate that eyewall convection releases latent heat prior to the convective burst.

[59] In a strong tropical cyclone, a 12-h-long convective burst appears to be able to cause intensification of $\geq$16 m s^{-1} in about 12 h, which would qualify as rapid intensification even if no further intensification occurred during the rest of the 24-h period. A convective burst in a weak tropical cyclone appears able to cause intensification of $\geq$9 m s^{-1} in about 12 h (half of the 24-h rapid intensification threshold in half of a 24-h period). The same amount of latent heat release causes more intensification in a strong tropical cyclone because a strong tropical cyclone has about a 2.5-times greater efficiency at converting released latent heat into increased tangential kinetic energy.

[60] Ignoring boundary layer processes (increases in ocean surface enthalpy flux and friction), a 12-h-long convective burst would drastically increase intensity by 14–27 m s^{-1} (27–52 knots). This estimate, however, appears too high because it ignores the increase in ocean surface friction during the ~12 h of intensification. More conservatively, the intensity increase would be smaller (9–16 m s^{-1}) if one ignores the increase in enthalpy while considering the increase in friction during the intensification period. Friction's detrimental effect on intensity is immediate and relatively easy to estimate while the beneficial effect of increased enthalpy flux is harder to estimate and subject to a time lag. Owing to complications such as this one, it is left to future studies to propose more complete ways to handle increased friction and enthalpy flux.

[61] The intensification estimated in this study's "energy pipeline" framework is subject to a factor of 2.3 uncertainty due to uncertainty in the input parameters that define the convective burst and the tropical cyclone's inner core. This uncertainty could be reduced if future studies improve estimates of the drag at the ocean surface, estimates of the three-dimensional tangential wind field's variation with intensity, or estimates of the surface rain rate under the eyewall, among other factors.

Appendix A: Increase in Friction During the Intensification Period

[62] This section calculates the extra energy loss due to the increase in ocean surface inner-core friction during a period of tropical cyclone wind intensification. In equation (A1), initial intensity I_i (m s^{-1}) increases to $I(t)$ after time t (s) elapses:

$$y(t) = \frac{I(t)}{I_i}. \tag{A1}$$

[63] The fractional increase in intensity at time t is $y(t)$. The H*wind analysis is used to fit a power law exponent e_3 relating the change in intensity to the change from initial frictional flux F_i (J s^{-1}) to frictional flux $F(t)$ (J s^{-1}) at time t:

$$F(t) = F_i\, y(t)^{e_3}. \tag{A2}$$

[64] Intensity is assumed to increase linearly with time to simplify the derivation. A constant rate of intensity increase is a simplification, even for a fairly short period such as 12 h. *Hack and Schubert* [1986, Figure 6] do show approximately constant intensification over 12 h in a model that shows significantly nonconstant intensification over 1 or 2 days. For simplicity, equation (A3) assumes that the period of intensification is 12 h long, i.e., equal in duration to the 12 h period during which latent heat is released inside of the convective burst:

$$\begin{aligned} c &= \frac{I_f - I_i}{t_{burst}}, \\ I(t) &= I_i + c\,t. \end{aligned} \tag{A3}$$

The definition of $I(t)$ in equation (A3) can be substituted back into equation (A1) and the result substituted into equation (A2):

$$\begin{aligned} y(t) &= 1 + \frac{c}{I_i}t, \\ F(t) &= F_i\left(1 + \frac{c}{I_i}t\right)^{e_3}. \end{aligned} \tag{A4}$$

[65] Next, the extra amount of frictional energy loss $\Delta E_{friction}$ (J) is calculated. The extra energy loss is the integral of frictional flux increase, $F(t) - F_i$, with respect to time. This integration is integration of the form $x^b - 1$ with respect to t where $x = 1 + at$:

$$\begin{aligned} \Delta E_{friction} &= \int_0^{t_{burst}} (F(t) - F_i)dt, \\ &= F_i \int_0^{t_{burst}} \left[\left(1 + \frac{c}{I_i}t\right)^{e_3} - 1\right]dt, \\ &= F_i \left[\frac{y(t)^{e_3+1}}{\frac{c}{I_i}(e_3+1)} - t\right]\Bigg|_{t=0}^{t=t_{burst}}. \end{aligned} \tag{A5}$$

[66] The definite integral in equation (A5) is evaluated, like terms combined, and $(y-1)/t_{burst}$ substituted for c/I_i. The result is equation (A6), in which y is shorthand for $y(t_{burst})$:

$$\Delta E_{friction} = F_i\; t_{burst}\left[\frac{1}{e_3+1}\frac{(y^{e_3+1}-1)}{(y-1)} - 1\right]. \tag{A6}$$

[67] The change in energy in equation (A6) is used in section 2.3.

Appendix B: Calculating 3-D Kinetic Energy

[68] It is easy to calculate the 3-D inner-core kinetic energy from $v_{700\text{hPa}}$ (m s^{-1}), the 700 hPa wind speed, if one assumes no altitude variation in the tangential wind. This rough estimate is designated $KE_{700\text{hPa}}$ (J).

[69] This appendix uses two methods to improve $KE_{700\text{hPa}}$ by calculating a scaling factor s_0 (unitless) that para-

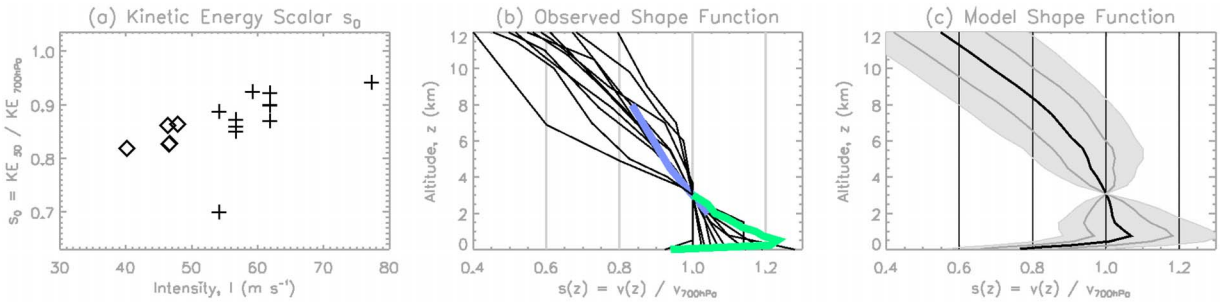

Figure B1. The vertical variation of tangential wind speed in the vicinity of the radius of maximum wind. (a) Integrating from the surface to 12 km altitude, the ratio of the actual kinetic energy to the kinetic energy were the tangential wind equal at all altitudes to the 700 hPa tangential wind. The plus symbols come from the one-dimensional profiles in Figure B1b. The diamonds come from five time steps of the simulation of *Braun et al.* [2006] that are summarized in Figure B1c. (b) The vertical profile of tangential wind speed as reported in previous studies listed in the first seven rows of Table 2. The one-dimensional wind speed profiles have been normalized by their 700 hPa wind speed to represent the shape function $s(z)$ used in equation (B4). The green line indicates the mean dropsonde profile of *Franklin et al.* [2003, Figure 8]. The blue line indicates the mean Doppler radar profile from aircraft observations analyzed by *Stern and Nolan* [2009, Figure 8c]. (c) The vertical profile of tangential wind speed within 70 km of the eye's center from the MM5 simulation described by *Braun* [2006]. Each grid cell's profile is normalized by that grid cell's 700 hPa tangential wind speed. The gray region indicates the middle 80% of the distribution at each altitude, the gray lines the middle 50% of the distribution, and the thick black line the median.

meterizes the effect of the vertical variation in tangential velocity:

$$KE_{3D} = s_0\ KE_{700\,\mathrm{hPa}}. \tag{B1}$$

The "improved" estimate of inner-core 3-D kinetic energy is designated KE_{3D} (J).

[70] The first method estimates the scaling factor using several time steps of an MM5 simulation of Hurricane Bonnie (1998) and finds s_0 to be fairly close to 1 (i.e., 0.8 to 0.9). These calculations are shown as diamonds in Figure B1a. This method takes into account the slope of the radius of maximum wind with altitude. This MM5 simulation is described by *Braun* [2006].

[71] The second method uses vertical profiles from several studies of tropical cyclones and finds a similar range of 0.88 ± 0.05 for s_0. These calculations are made for the tropical cyclones listed in Table 2 (first through seventh rows) and are shown as plus signs in Figure B1a. This second method does not take into account the outward slope of the radius of maximum wind, but it has the advantage that it can be applied to an individual vertical profile from a tropical cyclone rather than requiring a 3-D wind field. The vertical profiles used to calculate the plus signs in Figure B1a are shown in Figure B1b. For comparison, the simulated vertical variation in Hurricane Bonnie is shown in Figure B1c, and it agrees in its large-scale features with the observed profiles shown in Figure B1b.

[72] To calculate s_0 with either of the two above-mentioned methods, one begins with the general definition of kinetic energy KE (J) for any velocity v (m s^{-1}):

$$KE(v) = \frac{1}{2}\rho\ \mathrm{v}^2. \tag{B2}$$

When a 3-D wind field is available from a model, one can calculate s_0 via method 1:

$$s_0[\mathrm{model}] = \frac{\iiint\limits_{\text{inner core}} KE(v(x,y,z))}{\iiint\limits_{\text{inner core}} KE(v_{700\,\mathrm{hPa}}(x,y))} = \frac{KE_{3D}}{KE_{700\,\mathrm{hPa}}}. \tag{B3}$$

When one has instead an observed vertical profile of velocity $v(z)$ (m s^{-1}), then s_0 can be calculated via method 2:

$$s_0[\mathrm{obs}] = \frac{\int\limits_{\text{vertical profile}} KE(v_{700\,\mathrm{hPa}}\, s(z))}{\int\limits_{\text{vertical profile}} KE(v_{700\,\mathrm{hPa}})},$$
$$s_0[\mathrm{obs}] = \frac{\int_0^{12\,\mathrm{km}} \rho(z) s^2(z)}{m}. \tag{B4}$$

[73] Before using equation (B4), each observed profile is expressed as the product of a unitless shape function $s(z)$ times that profile's 700 hPa wind speed $v_{700\mathrm{hPa}}$ (m s^{-1}). The shape functions are plotted in Figure B1b for the observed profiles used in this study. The column mass from the surface to 12 km altitude is m (kg m^{-2}).

[74] **Acknowledgments.** TRMM satellite data was provided by NASA and JAXA. H*wind analysis provided by NOAA's Hurricane Research Division. The first author would like to thank his Ph.D. advisor, Michael Summers, for providing feedback on early results related to this study. The first author was supported through NASA grant NNX07AJ22A. The second author was supported in part by NASA grant NNH08ZDA001N-HRSP. Both authors would like to thank Ramesh Kakar for his continued

support of TRMM. Three anonymous reviewers provided suggestions that significantly strengthened this text. Computational facilities were provided by the Precipitation Processing System at NASA Goddard.

References

Andreas, E. L., and K. A. Emanuel (2001), Effects of sea spray on tropical cyclone intensity, *J. Atmos. Sci.*, *58*, 3741–3751, doi:10.1175/1520-0469(2001)058<3741:EOSSOT>2.0.CO;2.

Bevington, P. R., and D. K. Robinson (1992), *Data Reduction and Error Analysis for the Physical Sciences*, 2nd ed., McGraw Hill, New York.

Bohren, C. F., and B. A. Albrecht (1998), *Atmospheric Thermodynamics*, Oxford Univ. Press, New York.

Braun, S. A. (2006), High-resolution simulation of Hurricane Bonnie (1998), Part II: Water budget, *J. Atmos. Sci.*, *63*, 43–64, doi:10.1175/JAS3609.1.

Braun, S. A., M. T. Montgomery, and Z. Pu (2006), High-resolution simulation of Hurricane Bonnie (1998), Part I: The organization of eyewall vertical motion, *J. Atmos. Sci.*, *63*, 19–42, doi:10.1175/JAS3598.1.

Dodge, P., R. W. Burpee, and F. D. Marks (1999), The kinematic structure of a hurricane with sea level pressure less than 900 mb, *Mon. Weather Rev.*, *127*, 987–1004, doi:10.1175/1520-0493(1999)127<0987:TKSOAH>2.0.CO;2.

Emanuel, K. (1997), Some aspects of hurricane inner-core dynamics and energetics, *J. Atmos. Sci.*, *54*, 1014–1026, doi:10.1175/1520-0469(1997)054<1014:SAOHIC>2.0.CO;2.

Emanuel, K. (2003), Tropical cyclones, *Annu. Rev. Earth Planet. Sci.*, *31*, 75–104, doi:10.1146/annurev.earth.31.100901.141259.

Fierro, A. O., X.-M. Shao, and T. Hamlin (2011), Evolution of eyewall convective events as indicated by intra-cloud and cloud-to-ground lightning activity during the rapid intensification of hurricanes Rita and Katrina, *Mon. Weather Rev.*, *139*, 1492–1504, doi:10.1175/2010MWR3532.1.

Franklin, J. L., S. J. Lord, S. E. Feuer, and F. D. Marks (1993), The kinematic structure of Hurricane Gloria (1985) determined from nested analyses of dropwindsonde and Doppler radar data, *Mon. Weather Rev.*, *121*, 2433–2451, doi:10.1175/1520-0493(1993)121<2433:TKSOHG>2.0.CO;2.

Franklin, J. L., M. L. Black, and K. Valde (2003), GPS dropwindsondes wind profiles in hurricanes and their operational implications, *Weather Forecasting*, *18*, 32–44, doi:10.1175/1520-0434(2003)018<0032:GDWPIH>2.0.CO;2.

Fudeyasu, H., and Y. Wang (2011), Balanced contribution to the intensification of a tropical cyclone simulated in TCM4: Outer core spin-up process, *J. Atmos. Sci.*, *68*, 430–449, doi:10.1175/2010JAS3523.1.

Gamache, J. F., R. A. Houze, and F. D. Marks (1993), Dual-aircraft investigation of the inner core of Hurricane Norbert. Part III: Water budget, *J. Atmos. Sci.*, *50*, 3221–3243, doi:10.1175/1520-0469(1993)050<3221:DAIOTI>2.0.CO;2.

Gentry, R. C., T. T. Fujita, and R. C. Sheets (1970), Aircraft, spacecraft, satellite, and radar observations of Hurricane Gladys, 1968, *J. Appl. Meteorol.*, *9*, 837–850, doi:10.1175/1520-0450(1970)009<0837:ASSARO>2.0.CO;2.

Glickman, T. S. (Ed.) (2000), *Glossary of Meteorology*, 2nd ed., Am. Meteorol. Soc., Boston, Mass.

Guimond, S. R., G. M. Heymsfield, and F. J. Turk (2010), Multiscale observations of Hurricane Dennis (2005), The effects of hot towers on rapid intensification, *J. Atmos. Sci.*, *67*, 633–654, doi:10.1175/2009JAS3119.1.

Hack, J. J., and W. H. Schubert (1986), Nonlinear response of atmospheric vortices to heating by organized cumulus convection, *J. Atmos. Sci.*, *43*, 1559–1573, doi:10.1175/1520-0469(1986)043<1559:NROAVT>2.0.CO;2.

Hawkins, H. F., and S. M. Imbembo (1976), The structure of a small, intense hurricane—Inez 1966, *Mon. Weather Rev.*, *104*, 418–442, doi:10.1175/1520-0493(1976)104<0418:TSOASI>2.0.CO;2.

Hennon, P. A. (2006), The role of the ocean in convective burst initiation: Implications for tropical cyclone intensification, Ph.D. dissertation, Ohio State Univ., Columbus, Ohio.

Heymsfield, A. J., and L. J. Donner (1990), A scheme for parameterizing ice-cloud water content in general circulation models, *J. Atmos. Sci.*, *47*, 1865–1877, doi:10.1175/1520-0469(1990)047<1865:ASFPIC>2.0.CO;2.

Heymsfield, A. J., and J. Iaquinta (2000), Cirrus crystal terminal velocities, *J. Atmos. Sci.*, *57*, 916–938, doi:10.1175/1520-0469(2000)057<0916:CCTV>2.0.CO;2.

Heymsfield, G. M., J. B. Halverson, J. Simpson, L. Tian, and T. P. Bui (2001), ER-2 Doppler radar investigation of the eyewall of Hurricane Bonnie during the convection and moisture experiment-3, *J. Appl. Meteorol.*, *40*, 1310–1330, doi:10.1175/1520-0450(2001)040<1310:EDRIOT>2.0.CO;2.

Holland, G. J. (1980), An analytic model of the wind and pressure profiles in hurricanes, *Mon. Weather Rev.*, *108*, 1212–1218, doi:10.1175/1520-0493(1980)108<1212:AAMOTW>2.0.CO;2.

Houze, R. A. (1993), *Cloud Dynamics*, Academic, San Diego, Calif.

Iguchi, T., T. Kozu, J. Kwiatkowski, R. Meneghini, J. Awaka, and K. Okamoto (2009), Uncertainties in the rain profiling algorithm for the TRMM Precipitation Radar, *J. Meteorol. Soc. Jpn.*, *87A*, 1–30, doi:10.2151/jmsj.87A.1.

Kaplan, J., and M. DeMaria (2003), Large-scale characteristics of rapidly intensifying tropical cyclones in the North Atlantic basin, *Weather Forecasting*, *18*, 1093–1108, doi:10.1175/1520-0434(2003)018<1093:LCORIT>2.0.CO;2.

Kelley, O. A., J. Stout, M. Summers, and E. J. Zipser (2010), Do the tallest convective cells over the tropical ocean have slow updrafts?, *Mon. Weather Rev.*, *138*, 1651–1672, doi:10.1175/2009MWR3030.1.

Kepert, J. D. (2010), Tropical cyclone structure and dynamics, in *Global Perspectives on Tropical Cyclones: From Science To Mitigation*, chap. 1, pp. 3–53, World Sci., Hackensack, N. J.

Knollenberg, R. G., K. Kelly, and J. C. Wilson (1993), Measurements of high number densities of ice crystals in the tops of tropical cumulonimbus, *J. Geophys. Res.*, *98*(D5), 8639–8664, doi:10.1029/92JD02525.

Kossin, J. P. (2002), Daily hurricane variability inferred from GOES infrared imagery, *Mon. Weather Rev.*, *130*, 2260–2270, doi:10.1175/1520-0493(2002)130<2260:DHVIFG>2.0.CO;2.

Kozu, T., T. Kawanishi, H. Kuroiwa, M. Kojima, K. Oikawa, H. Kumagai, K. Okamoto, M. Okumura, H. Nakatsuka, and K. Nishikawa (2001), Development of precipitation radar onboard the TRMM satellite, *IEEE Trans. Geosci. Remote Sens.*, *39*, 102–116, doi:10.1109/36.898669.

Kummerow, C., W. Barnes, T. Kozu, J. Shiue, and J. Simpson (1998), The Tropical Rainfall Measuring Mission (TRMM) sensor package, *J. Atmos. Oceanic Technol.*, *15*, 809–817, doi:10.1175/1520-0426(1998)015<0809:TTRMMT>2.0.CO;2.

Langousis, A., and D. Veneziano (2009), Theoretical model of rainfall in tropical cyclones for the assessment of long-term risk, *J. Geophys. Res.*, *114*, D02106, doi:10.1029/2008JD010080.

Lonfat, M., F. D. Marks, and S. S. Chen (2004), Precipitation distribution in tropical cyclones using the Tropical Rainfall Measuring Mission (TRMM) microwave imager: A global perspective, *Mon. Weather Rev.*, *132*, 1645–1660, doi:10.1175/1520-0493(2004)132<1645:PDITCU>2.0.CO;2.

Lyons, W. A., and C. S. Keen (1994), Observations of lightning in convective supercells within tropical storms and hurricanes, *Mon. Weather Rev.*, *122*, 1897–1916, doi:10.1175/1520-0493(1994)122<1897:OOLICS>2.0.CO;2.

Maclay, K. S., M. DeMaria, and T. H. Vonder Haar (2008), Tropical cyclone inner-core kinetic energy evolution, *Mon. Weather Rev.*, *136*, 4882–4898, doi:10.1175/2008MWR2268.1.

Malkus, J. S., and H. Riehl (1960), On the dynamics and energy transformations in steady-state hurricanes, *Tellus*, *12*, 1–20, doi:10.1111/j.2153-3490.1960.tb01279.x.

Marks, F. D., R. A. Houze, and J. F. Gamache (1992), Dual-aircraft investigation of the inner core of Hurricane Norbert, Part I: Kinematic structure, *J. Atmos. Sci.*, *49*, 919–942, doi:10.1175/1520-0469(1992)049<0919:DAIOTI>2.0.CO;2.

Molinari, J., and D. Vollaro (2010), Rapid intensification of a sheared tropical storm, *Mon. Weather Rev.*, *138*, 3869–3885, doi:10.1175/2010MWR3378.1.

Montgomery, M. T., M. E. Nicholls, T. A. Cram, and A. B. Saunders (2006), A vortical hot tower route to tropical cyclogenesis, *J. Atmos. Sci.*, *63*, 355–386, doi:10.1175/JAS3604.1.

Montgomery, M. T., N. Van Sang, R. K. Smith, and J. Persing (2009), Do tropical cyclones intensify by WISKE?, *Q. J. R. Meteorol. Soc.*, *135*, 1697–1714, doi:10.1002/qj.459.

Nolan, D. S., Y. Moon, and D. P. Stern (2007), Tropical cyclone intensification from asymmetric convection: Energetics and efficiency, *J. Atmos. Sci.*, *64*, 3377–3405, doi:10.1175/JAS3988.1.

Powell, M. D., S. H. Houston, L. R. Amat, and N. Morisseau-Leroy (1998), The HRD real-time hurricane wind analysis system, *J. Wind Eng. Ind. Aerodyn.*, *77/78*, 53–64.

Powell, M. D., P. J. Vickery, and T. A. Reinhold (2003), Reduced drag coefficient for high wind speeds in tropical cyclones, *Nature*, *422*, 279–283, doi:10.1038/nature01481.

Powell, M. D., E. W. Uhlhorn, and J. D. Kepert (2009), Estimating maximum surface winds from hurricane reconnaissance measurements, *Weather Forecasting*, *24*, 868–883, doi:10.1175/2008WAF2007087.1.

Powell, M. D., et al. (2010), Reconstruction of Hurricane Katrina's wind fields for storm surge and wave hindcasting, *Ocean Eng.*, *37*, 26–36, doi:10.1016/j.oceaneng.2009.08.014.

Pueschel, R. F., D. A. Allen, C. Black, S. Faisant, G. V. Ferry, S. D. Howard, J. M. Livingston, J. Redemann, C. E. Sorenson, and S. Verma (1995), Condensed water in tropical cyclone Oliver, 8 February 1993, *Atmos. Res.*, *38*, 297–313, doi:10.1016/0169-8095(95)00002-9.

Reasor, P. D., M. D. Eastin, and J. F. Gamache (2009), Rapidly intensifying Hurricane Guillermo (1997), Part I: Low-wavenumber structure and evolution, *Mon. Weather Rev.*, *137*, 603–631, doi:10.1175/2008MWR2487.1.

Riehl, H., and J. Malkus (1961), Some aspects of Hurricane Daisy, 1958, *Tellus*, *13*, 181–213, doi:10.1111/j.2153-3490.1961.tb00077.x.

Ritchie, E. A., J. Simpson, W. T. Liu, J. Halverson, C. Velden, K. F. Brueske, and H. Pierce (2003), Present day satellite technology for hurricane research, in *Hurricane!: Coping With Disaster*, edited by R. H. Simpson et al., pp. 248–891, AGU, Washington, D. C.

Rodgers, E., W. Olson, J. Halverson, J. Simpson, and H. Pierce (2000), Environmental forcing of Supertyphoon Paka's (1997) latent heat structure, *J. Appl. Meteorol.*, *39*, 1983–2006, doi:10.1175/1520-0450(2001)040<1983:EFOSPS>2.0.CO;2.

Rogers, R. (2010), Convective-scale structure and evolution during a high-resolution simulation of tropical cyclone rapid intensification, *J. Atmos. Sci.*, *67*, 44–70, doi:10.1175/2009JAS3122.1.

Schmitt, C. G., and A. J. Heymsfield (2009), The size distribution and mass-weighted terminal velocity of low-altitude tropopause cirrus crystal populations, *J. Atmos. Sci.*, *66*, 2013–2028, doi:10.1175/2009JAS3004.1.

Schubert, W. H., C. M. Rozoff, J. L. Vigh, B. D. McNoldy, and J. P. Kossin (2007), On the distribution of subsidence in the hurricane eye, *Q. J. R. Meteorol. Soc.*, *133*, 595–605, doi:10.1002/qj.49.

Seto, S., and T. Iguchi (2007), Rainfall-induced changes in actual surface backscattering cross sections and effects on rain-rate estimates by spaceborne precipitation radar, *J. Atmos. Oceanic Technol.*, *24*, 1693–1709, doi:10.1175/JTECH2088.1.

Shapiro, L. J., and M. T. Montgomery (1993), A three-dimensional balance theory for rapidly rotating vortices, *J. Atmos. Sci.*, *50*, 3322–3335, doi:10.1175/1520-0469(1993)050<3322:ATDBTF>2.0.CO;2.

Shin, S., and R. K. Smith (2008), Tropical-cyclone intensification and predictability in a minimal three-dimensional model, *Q. J. R. Meteorol. Soc.*, *134*, 1661–1671, doi:10.1002/qj.327.

Smith, R. K., M. T. Montgomery, and N. Van Sang (2009), Tropical cyclone spin-up revisited, *Q. J. R. Meteorol. Soc.*, *135*, 1321–1335, doi:10.1002/qj.428.

Soloviev, A., and R. Lukas (2010), Effects of bubbles and sea spray on air-sea exchange in hurricane conditions, *Boundary Layer Meteorol.*, *136*, 365–376, doi:10.1007/s10546-010-9505-0.

Steranka, J., E. B. Rodgers, and R. C. Gentry (1986), The relationship between satellite measured convective bursts and tropical cyclone intensification, *Mon. Weather Rev.*, *114*, 1539–1546, doi:10.1175/1520-0493(1986)114<1539:TRBSMC>2.0.CO;2.

Stern, D. P., and D. S. Nolan (2009), Reexamining the vertical structure of tangential winds in tropical cyclones: Observations and theory, *J. Atmos. Sci.*, *66*, 3579–3600, doi:10.1175/2009JAS2916.1.

Van Sang, N., R. K. Smith, and M. T. Montgomery (2008), Tropical-cyclone intensification and predictability in three dimensions, *Q. J. R. Meteorol. Soc.*, *134*, 563–582, doi:10.1002/qj.235.

Vickery, P. J., and D. Wadhera (2008), Statistical models of Holland pressure profile parameter and radius to maximum winds of hurricanes from flight-level pressure and H*wind data, *J. Appl. Meteorol. Climatol.*, *47*, 2497–2517, doi:10.1175/2008JAMC1837.1.

Vickery, P. J., D. Wadhera, M. D. Powell, and Y. Chen (2009), A hurricane boundary layer and wind field model for use in engineering applications, *J. Appl. Meteorol. Climatol.*, *48*, 381–405, doi:10.1175/2008JAMC1841.1.

Wallace, J. M., and P. V. Hobbs (2006), *Atmospheric Science: An Introductory Survey*, 2nd ed., Elsevier, Amsterdam.

Willoughby, H. E. (1998), Tropical cyclone eye thermodynamics, *Mon. Weather Rev.*, *126*, 3053–3067, doi:10.1175/1520-0493(1998)126<3053:TCET>2.0.CO;2.

Willoughby, H. E., and M. E. Rahn (2004), Parametric representation of the primary hurricane vortex, part I: Observations and evaluation of the Holland (1980) model, *Mon. Weather Rev.*, *132*, 3033–3048, doi:10.1175/MWR2831.1.

Zipser, E. J. (2003), Some view on "hot towers" after 50 years of tropical field programs and two years of TRMM data, in *Cloud Systems, Hurricanes, and the TRMM*, *Meteorol. Monogr.*, vol. 51, edited by W.-K. Tao and R. Adler, pp. 49–58, Am. Meteorol. Soc., Boston, Mass.

Zou, X., Y. Wu, and P. S. Ray (2010), Verification of a high-resolution model forecast using airborne Doppler radar analysis during the rapid intensification of Hurricane Guillermo, *J. Appl. Meteorol. Clim.*, *49*, 807–820, doi:10.1175/2009JAMC2182.1.

J. B. Halverson, Joint Center for Earth Systems Technology, University of Maryland Baltimore County, Baltimore, MD 21250, USA.

O. A. Kelley, NASA Goddard Space Flight Center, Code 610.2, Bldg. 32, Rm. S048B, Greenbelt, MD 20771, USA. (owen.kelley@nasa.gov)